Correspondence to:
J. Ren,
jiaenren@umich.edu

Statistical Characteristics of Polar Cap Patches Observed by RISR-C

Jiaen Ren[1] 📷, Shasha Zou[1] 📷, Robert G. Gillies[2] 📷, Eric Donovan[2] 📷, and Roger H. Varney[3] 📷

[1]Climate and Space Sciences and Engineering Department, University of Michigan, Ann Arbor, MI, USA, [2]Department of Physics and Astronomy, University of Calgary, Calgary, Alberta, Canada, [3]Center for Geospace Studies, SRI international, Menlo Park, CA, USA

Abstract Polar cap "patches" are ~100 to 1,000 km islands of high-density plasma at polar latitudes, which can cause scintillation to communication and navigation signals. An automatic algorithm for patch identification has been developed and applied to the observations from the Resolute Bay Incoherent Scatter Radar-Canada during January to March and September to December, 2016. Four hundred thirty-seven patches have been identified, and their statistical characteristics have been studied, including their occurrence rate as a function of magnetic local time (MLT) and statistical profiles of plasma parameters at different MLT sectors. About 60% of the patches are observed between 1200 and 2400 MLT, consistent with earlier observations near this latitude (~82° MLat) using different instruments. Superposed epoch analysis has been used to study the vertical profiles of electron density and temperature, ion temperature, vertical velocity, and flux measured within the patches where the density peaks. The patch median density is higher than the sector median with a ratio of ~1.8–2.1 at the altitude of F-region density peak. Meanwhile, the patch electron temperature is typically lower than the sector median between ~200 and 450 km with the largest difference near noon (~380 K). In contrast, the ion temperature profile of the patches does not show obvious differences except in the noon sector, where the ion temperature is about 150 K higher than the sector median at ~360 km. Additionally, downward ion fluxes with peak exceeding ~10^{13} m^{-2} s^{-1} are found in the patches between ~200 and 400 km at all MLT sectors.

1. Introduction

Since the polar cap patches were discovered by Weber et al. (1984) and then defined by Crowley (1996) as islands of high-density ionospheric plasma surrounded by plasma of half or less density in the F-region ionosphere, their generation mechanism and evolution process, as well as their impact on modern technology has been constantly studied. The reason why understanding of this phenomenon is so important is that polar cap patches are generally viewed as the main reason for disturbances in navigation and communication signals in the polar regions (Basu et al., 1987, 1988). The sizes of the irregularities within patches scale from hundreds of kilometers to 10 m, and their density can reach as large as 10^6 cm^{-3}, corresponding to ~9 MHz F2 layer critical frequency (Carlson, 2012, and references therein). They may also disrupt trans-ionospheric radio waves at MHz-GHz frequencies, which includes radio frequency systems varying from military and governmental HF communication to satellite UHF communication and Global Navigation Satellite Systems.

The generation of the polar cap patches requires both a reservoir of high-density plasma and a segmentation mechanism to isolate the large-scale plasma into smaller patches. One major source of the patches is the storm-enhance density (SED) in the dayside subauroral region, where those high-density plasma are produced by the solar EUV radiation (Foster, 1993). Patches can be segmented by variations of the high-latitude ionosphere convection pattern due to temporal changes in the interplanetary magnetic field (IMF) B_z component (Anderson et al., 1988; Tsunoda, 1988) and B_y component (Sojka et al., 1993, 1994), or by transient magnetopause reconnection (Carlson et al., 2006; Lockwood & Carlson, 1992). Imager and radar observations have shown that some patches associated with localized flow channels can originate from poleward moving auroral forms (Wang et al., 2016), which are usually seen as a result of transient reconnection, and the patch structuring processes have dependence on the IMF B_y condition (Zhang et al., 2011). Soft particle precipitation near the cusp can be another source of plasma density enhancement, which can then be isolated into patches by high-speed plasma flow channels associated with IMF B_y reversals (Rodger et al., 1994). While many mechanisms have been proposed for the patch formation, it is not clear yet which produces most of the patches observed.

Statistical properties of the polar cap patches will potentially show key information regarding their formation mechanisms and propagation processes. Statistically, enhancement of electron temperature within the patch would indicate that the patch is generated by particle precipitation, while a decrease in the electron temperature would suggest that the plasma enhancement is generated on the dayside due to solar EUV radiation and then propagates to its current location. Observations have shown that the electron temperature within the dayside SED and SED plume is lower than the surrounding regions (e.g., Foster et al., 2005; Zou et al., 2013, 2014). Weber et al. (1984) observed approximately seven plasma patches with sizes of 800–1,000 km drifting antisunward using an all-sky imaging photometer and an ionosonde. Combined with simultaneous particle measurements taken by Dynamic Explorer 2 satellite, they showed that these patches are not generated locally but near the dayside auroral zone because of the absence of accelerated and structured electron precipitation. However, there have not been any systematic studies on the patch plasma characteristics.

Previous statistical studies on the polar cap patches have used database from satellites (e.g., Coley & Heelis, 1995; Noja et al., 2013), meridian scanning photometers (MSP, e.g., McEwen & Harris, 1996; Moen et al., 2007), and all-sky imagers (e.g., Hosokawa et al., 2009) to study their drift motion and occurrence frequency at different universal times (UT) and local times (LT). Based on ion density measurement taken by the Dynamic Explorer 2 spacecraft, Coley and Heelis (1995) developed an automatic technique to identify polar cap patches, followed by a statistical study of 281 patches showing a preferred patch horizontal size of ~300–400 km and an occurrence frequency peak around winter solstice and between ~12–20 UT in the northern hemisphere (NH). Sojka et al. (1994) used Utah State University time-dependent ionospheric model to simulate the seasonal and UT variation of patch formation by modulating the IMF B_y component. Their results predicted an absence of patches between 8 UT and 12 UT and most intense patches between 20 UT and 24 UT at winter solstice in the NH. These model predictions are later confirmed by total electron content (TEC) observations from satellites (David et al., 2016). McEwen and Harris (1996) analyzed 523 patches observed by meridian-scanning photometer at Eureka, Canada during winters from 1990 to 1994. They found that more patches are observed during local evening hours than the morning hours, and most of the patches occurred during or ~1–2 hr after negative IMF B_z conditions. More recently, Noja et al. (2013) analyzed GPS TEC observations from the CHAMP satellite during 2001–2004 and reported higher patch occurrence was found at the dayside polar cusp and dusk side at ~80° MLat. In their results, more patches were observed between 1400 MLT to 2100 MLT near RISR site. Spicher et al. (2017) used Swarm satellites observation during 2013–2016 and showed that the patch occurrence rate was enhanced during local winter and reduced during local summer for both hemispheres. They also showed that more patches were observed in the dusk (dawn) sector for negative (positive) IMF B_y condition.

Hosokawa et al. (2009) investigated the motion of 561 individual polar cap patches observed from 2005 to 2007, using all-sky airglow imagers at Resolute Bay. They demonstrated that the dawn-dusk component of the patch's drift velocity is mainly controlled by polarity of the IMF B_y component. In addition, they found that the patches tend to drift towards dusk even when IMF B_y equals 0, which is consistent with the fact that typically the dusk convection cell is bigger than the dawn cell due to the conductivity effect (Atkinson & Hutchison, 1978; Ruohoniemi & Greenwald, 1996, 2005). Moreover, Moen et al. (2007) used 8-year data from MSP at Svalbard and observed 333 patches in 43 days that exited the polar cap during nighttime. They found a nearly symmetric bell-shape distribution of patch occurrence centered around 23:25 MLT, which is likely caused by the tendency of patch motion from dawn to dusk. In a recent study by Zou et al. (2015), 97 patches were observed by an all-sky imager at Resolute Bay with simultaneous flow measurements by Super Dual Auroral Radar Network during the northern winter months from 2008 to 2012. Localized flow enhancements were found to be associated with ~67% of the patches with a typical flow speed of 600 m/s, in favor of IMF B_y-dominated conditions.

While a good understanding of patch size and occurrence distribution in terms of season and time (UT or MLT) has been developed by these previous statistical studies, more detailed statistical plasma characteristics within the patches, such as their vertical profiles of density and plasma temperature, are not well-known so far. Fortunately, the newly deployed Resolute Bay Incoherent Radar (RISR) provides such a capability. Perry (2015) used a patch detection algorithm on the northern face of the RISR (RISR-N) data measured during 5 days each in March and December in 2010, and reported distributions of F-region plasma density and temperatures of the patches, but the statistical profiles within the patches were not studied. In our work, based

on 7-month measurements taken by the Canadian component of the RISR radars (RISR-C; Gillies et al., 2016) in 2016, we developed an automatic algorithm to identify the polar cap patches and constructed a database of 437 patches. We then studied the MLT distribution of patch occurrence frequency and also conducted a superposed epoch analysis on altitude profiles of plasma density, temperature, and ion fluxes measured within the patches.

2. Instrumentation and Data

2.1. RISR-C Database

The polar cap patches have been observed for more than 30 years by several types of measurements, such as ionosonde, coherent and incoherent scatter radar (ISR), all-sky imager, ionospheric tomography, and in situ measurements from satellite and sounding rockets. Among those instruments, the ISR stands out with its unique ability to measure the vertical profiles of electron density, electron and ion temperature, and ion line-of-sight (LOS) velocity simultaneously.

Resolute Bay is currently the highest geomagnetic latitude (82.43°) ISR station (74.73°N, 94.91°W geographic) in the world, making it an ideal place for polar cap patch observation. The RISR-C database used in this study contains measurements from January to March and from September to December in 2016, with a total observational time of ~1,100 hr. During the 7 months, the radar operated for several selected days in each month. All the RISR-C data from 2016 was collected during coordinated experiments with RISR-N, but only RISR-C data are used in this paper because we aim to study the patch profile along the field-aligned direction, which is within the RISR-C field of view and outside the RISR-N field of view.

In each run, the radar provides measurements of electron density, electron and ion temperature, and ion LOS velocity from ~100 to ~700 km in altitude, with a spatial resolution of ~24 km (long pulse mode) and a time resolution of 1 min. Raw electron density directly obtained from power without range integration or correction for measured electron and ion temperature ratios is also available with a spatial resolution of ~3 km.

In addition, since RISR uses a phased array of thousands of antenna element units to enable almost simultaneous multiple-beam measurements, its beam configuration can be changed on demand for each operation. As a result, there are in total four different beam configurations throughout the 7-month data set that were used in this study. In order to interpret the LOS velocity and other parameters in a straightforward and meaningful way, for each beam configuration we choose to use data obtained from the beam pointing most closely to the field-aligned direction, which is nearly vertical (169.09° azimuth, 86.41° elevation) at Resolute Bay. The beams that have been used in this study are 83.0° elevation and −157.0° azimuth, 85.0° elevation, and −157.0° azimuth and 90.0° elevation. Projections of ISR K vectors of these three beams on the field-aligned direction are around 0.997, 0.998, and 0.999, respectively.

2.2. Patch Identification Technique

Using the time series data of electron density observed by RISR-C, we developed an automatic algorithm to identify the patches and constructed a database of 437 patches. In the identification algorithm, a set of criteria listed below has been applied to effectively distinguish the features of a patch from other density enhancements shown in the data.

1. A patch should appear as a density peak in the F-region with a minimum prominence of $\log_{10}(2)$ in log scale, according to the classical definition that a patch has at least double density of its surrounding plasma (Crowley, 1996).
2. A patch should last at least 3 min but no more than 2 hr in the radar observation, given a typical patch size range of ~100–1,000 km (Coley & Heelis, 1995) and a patch convection velocity range of ~150–500 m/s that Hosokawa et al. (2009) reported at Resolute Bay. Density enhancement with shorter duration is regarded as noise, and those with longer duration can be most likely regarded as part of the tongue of ionization.
   To fulfill the term "*F-region*" in the first criterion, average raw electron density from 250 to 400 km is calculated at each time record, shown in log scale as black curve in the second panel of Figure 1. Based on the second criterion, a 3-point median filter has already been applied to remove high-frequency fluctuations. Then a peak-finding algorithm is applied to only identify those peaks with minimum prominences of $\log_{10}(2)$ within a temporal width of 2 hr. The ground level used to measure the prominence of a peak is
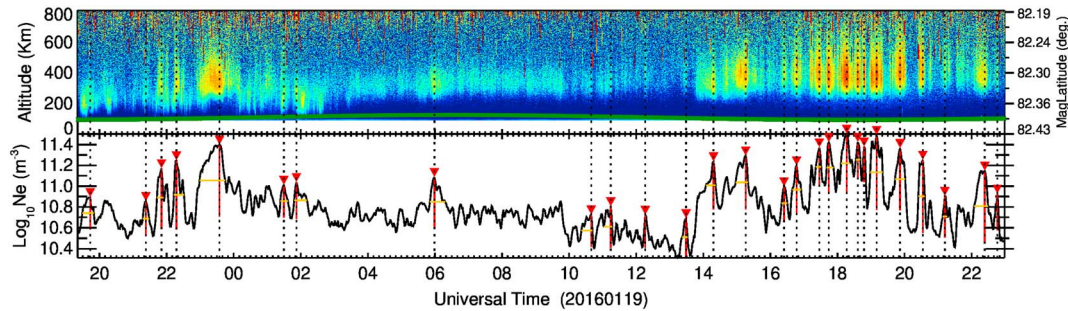
Figure 1. An example of patch identification procedure for Resolute Bay Incoherent Scatter Radar-Canada measurement on 19 January 2016. The first panel shows the electron density obtained directly from power with no range integration and no correction for measured temperature. In the second panel, black curve shows average electron density from 250 to 400 km with a 3-point median filter applied. The density peaks that fulfill the criteria mentioned in the text are marked by red triangles. Within each peak, the vertical red line and horizontal yellow line indicate its prominence and half-prominence width, respectively.

determined in this way: Find the minimum values in a 1-hr window before and after the peak position, respectively, then choose the higher one of the two minimum values to be the ground level. The half-prominence width indicates the duration between two edges of a patch moving over the radar site. We have applied this patch identification procedure to the entire data set, followed by a visual inspection. As a result, 437 patches have been identified, allowing us to analyze their statistical characteristics.

3. Statistical Results

3.1. MLT Dependence of Patch Occurrence

In Figure 2, the first panel presents the total measurement time of RISR-C at each MLT and corresponding UT. The second and third panels show the number of patches observed and patch occurrence frequency (in
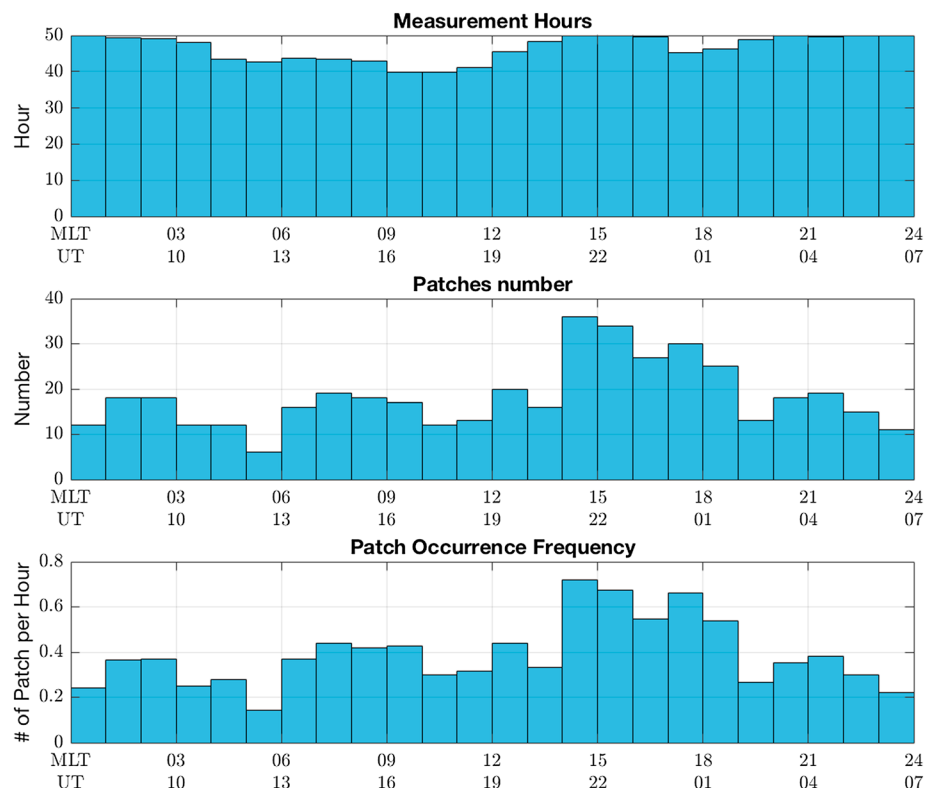

Figure 2. MLT and UT distribution of Resolute Bay Incoherent Scatter Radar-Canada measurement time, number of polar cap patches, and patch occurrence frequency. MLT = magnetic local time; UT = universal time.
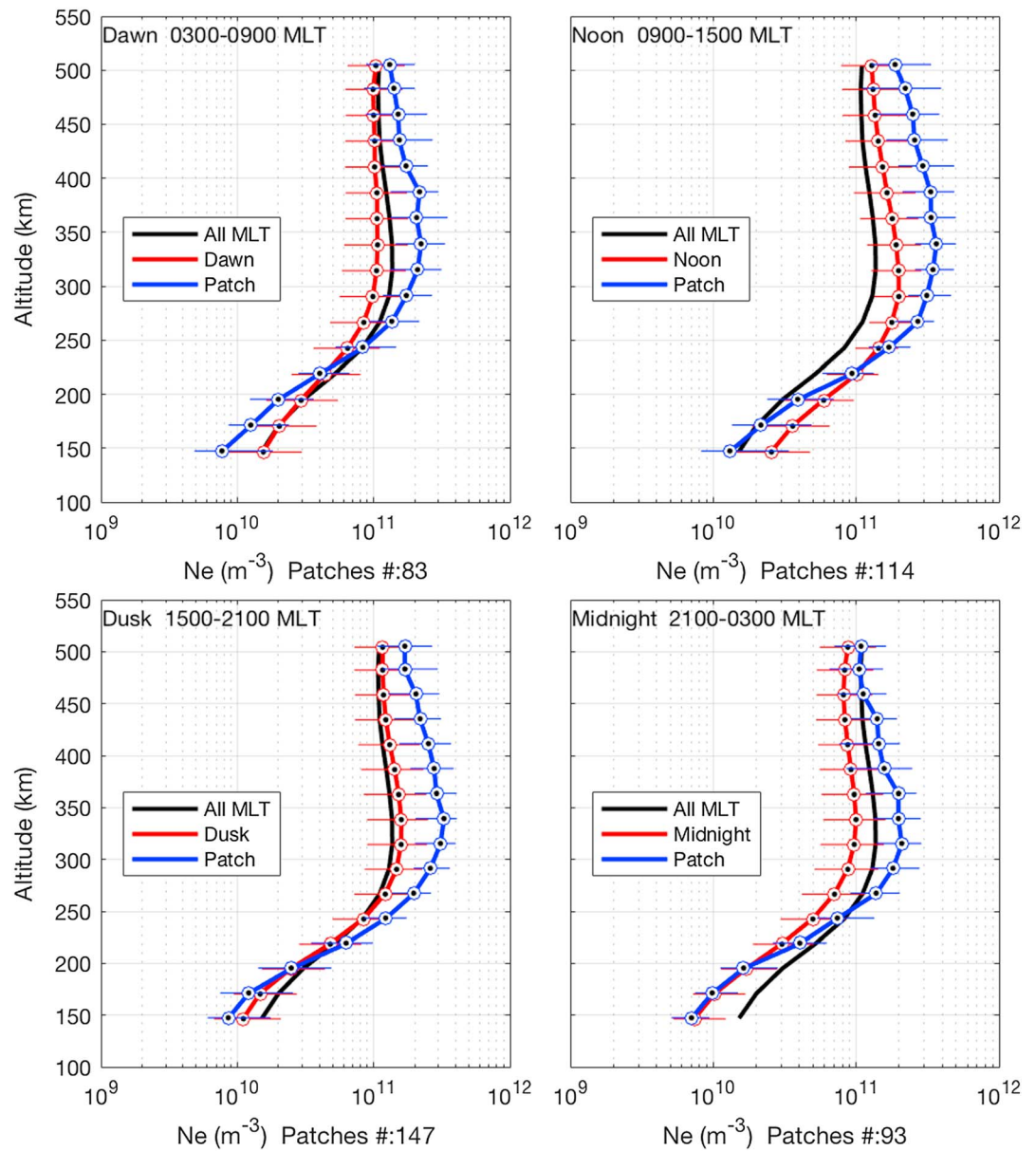
Figure 3. Electron density profiles measured in dawn (03–09 MLT), noon (09–15 MLT), dusk (15–21 MLT), and midnight (21–03 MLT) sector, respectively. The black curves represent the median profiles of measurements taken at all the MLTs. The red curves represent median profiles calculated using data only measured at each MLT sector. The blue curves represent median profiles measured at the density peaks of the patches observed in each sector. The horizontal bars (not shown for the black curves) indicate range from the first quartile (Q1) to the third quartile (Q3) of the corresponding data at each altitude. MLT = magnetic local time.

terms of number of patches observed per hour) at each MLT. In general, patches are observed more often in the afternoon sector between 1400 and 1900 MLT. About 35% of the patches are observed during this 5-hr period, and nearly 60% of them are observed between 12 and 24 MLT. The minimum patch occurrence frequency locates at 5–6 MLT with a value of one per 7.1 hr, while the maximum occurrence frequency one per 1.4 hr is found at 14–15 MLT, nearly 3.2 times of the frequency at 5–6 MLT.

3.2. Superposed Epoch Analysis of Patch Plasma Profiles

Figures 3–9 show the results of the superposed epoch analysis of the patch plasma profiles measured by RISR-C long pulse mode. At each altitude, the main curve represents the median value of all the
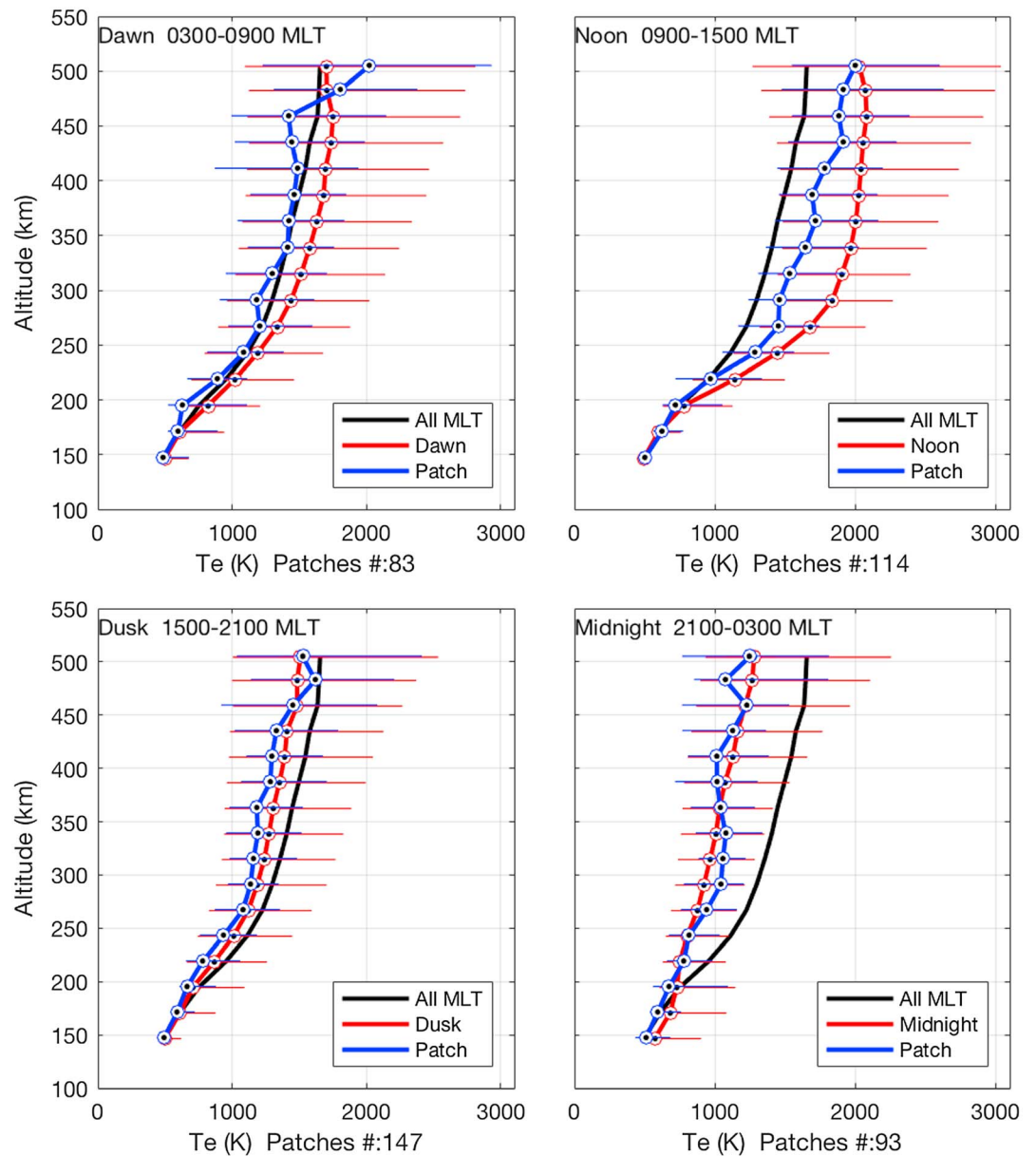
Figure 4. Electron temperature profiles measured in dawn (03–09 MLT), noon (09–15 MLT), dusk (15–21 MLT), and midnight (21–03 MLT) sectors, respectively. MLT = magnetic local time.

corresponding measurements taken at that altitude level, while the horizontal line denotes the range from the first quartile (Q1) to the third quartile (Q3). Beams used in this study are described in section 2.1.

First, the median profiles of electron density (N_e, Figure 3), electron temperature (T_e, Figure 4), ion temperature (T_i, Figure 5), ion line-of-sight velocity (LOS V_i, Figures 6 and 8) and flux (N_e times LOS V_i, Figures 7 and 9) from all the available measurements are calculated and plotted as the black curves in each figure. Then we separate the data into four sectors: dawn (03–09 MLT), noon (09–15 MLT), dusk (15–21 MLT), and midnight (21–03 MLT). For each sector, the median profiles of those five parameters are calculated and plotted as the red curves in each figure. At last, the median profiles measured at the density peaks of the patches observed in each sector are plotted as blue curves in each figure. To control the data quality while maintain adequate amount of data for statistical analysis, we filtered the density and temperature data by limiting the relative error to be less than 2. The measurement uncertainties are provided in RISR-C data set. For LOS
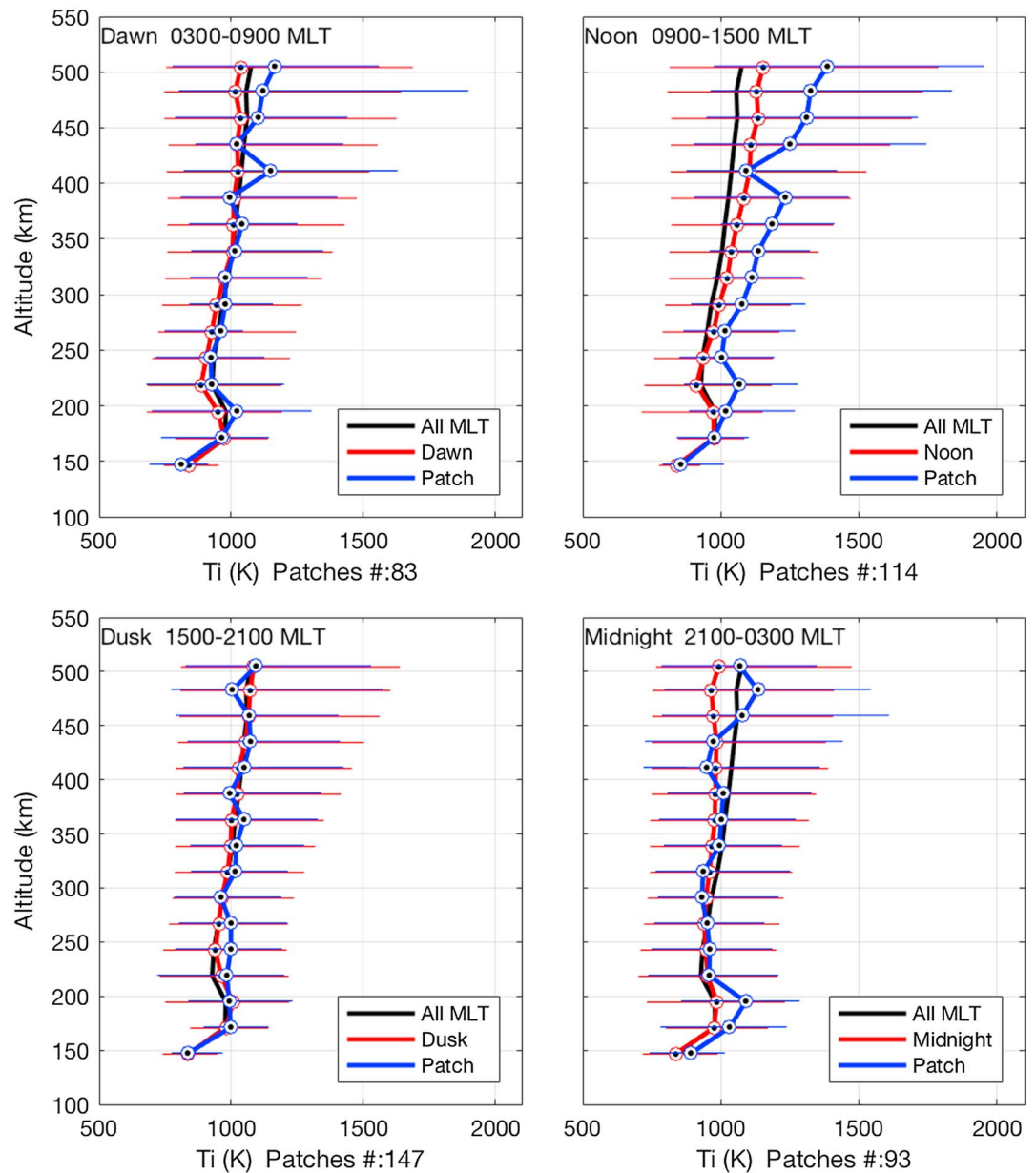
Figure 5. Ion temperature profiles measured in dawn (03–09 MLT), noon (09–15 MLT), dusk (15–21 MLT), and midnight (21–03 MLT) sector. MLT = magnetic local time.

velocity, since the relative errors are generally larger, the limit is increased to 4 to keep sufficient data, while another limit that the absolute error should be less than 400 m/s is also added to control quality of the data used in the study.

3.2.1. Electron Density Profile

As shown in Figure 3, compared with the overall median density, the sector median shows higher density in the noon and dusk sectors, and lower density in the dawn and midnight sectors, at almost all altitude levels. In all of the four sectors, the patch median plasma densities above 200 km are higher than the sector median plasma densities, as expected. The F-region density peak decreases from the dayside ($\sim 2.0 \times 10^{11}$ m^{-3} for the noon sector, $\sim 3.6 \times 10^{11}$ m^{-3} for patches) to the nightside ($\sim 1.0 \times 10^{11}$ m^{-3} for the midnight sector, $\sim 2.1 \times 10^{11}$ m^{-3} for patches), in agreement with the results by Perry (2015, Figure 4.12). The ratio of F-region density peak between the patches and the sector median is ~ 1.8 in the noon sector and ~ 2.1 in the dawn,
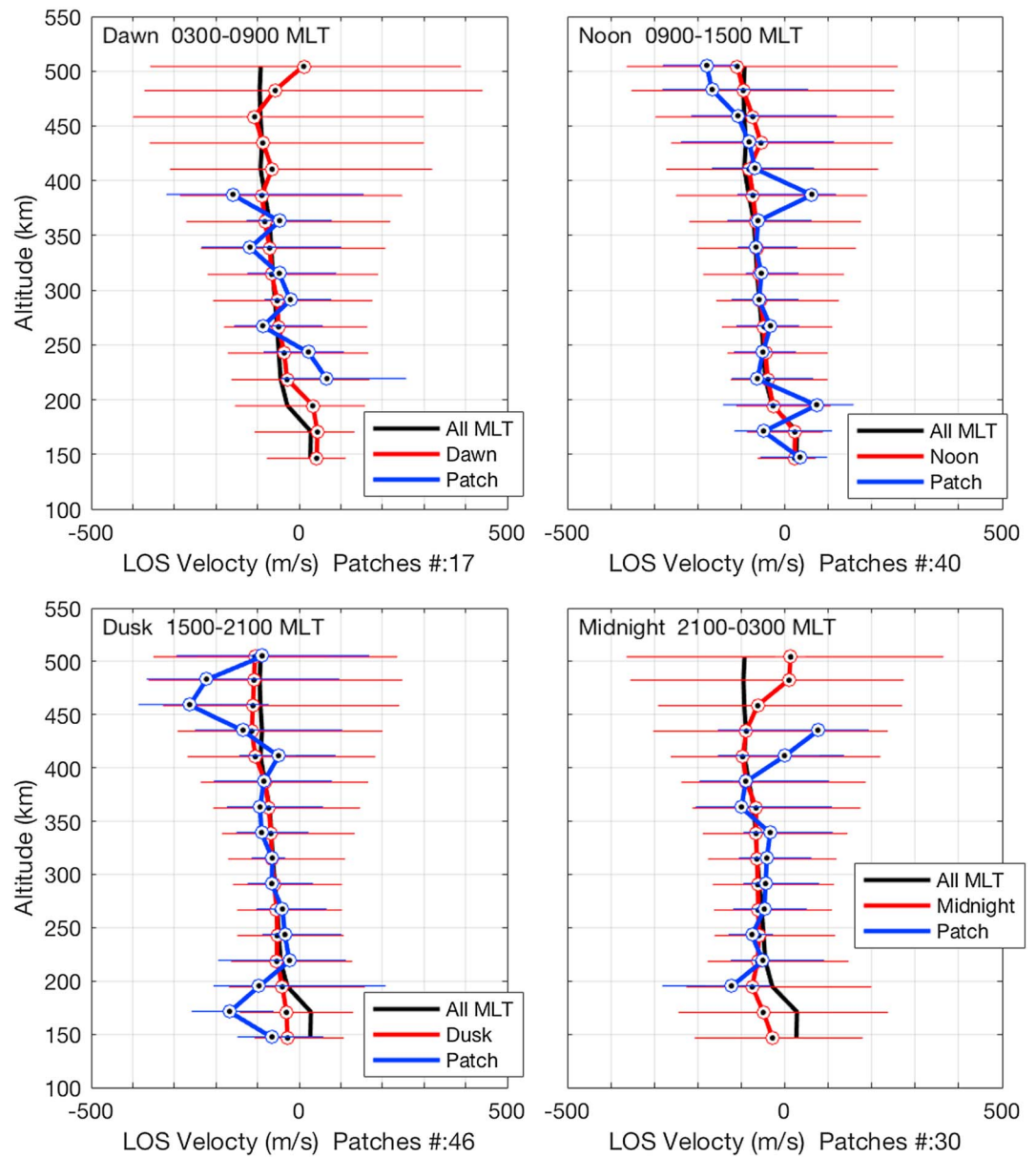
Figure 6. Line-of-sight ion velocity profiles measured in dawn (03–09 MLT), noon (09–15 MLT), dusk (15–21 MLT), and midnight (21–03 MLT) sector, using only the vertical beam (90° elevation angle). Negative (positive) line-of-sight velocity means downward (upward). The median profiles measured within the patches (blue curves) are fluctuating due to the small number of patches observed in each sector. MLT = magnetic local time.

dusk, and midnight sectors. The topside ionosphere density differences between the patch and the sector median decrease from the dayside to the nightside. Therefore, patch detection using LEO satellite in situ density above 450 km may not be very sensitive on the nightside. Also, it is noted that patch density is lower than the sector median density below ~200 km except on the nightside. This phenomenon has been seen in the SED event reported in Figure 8 in Zou et al. (2013) due to lifting of the storm-time F-region plasma to higher altitudes.

3.2.2. Electron Temperature Profile

As shown in Figure 4, comparing the overall median electron temperature with the sector medians, higher temperature reaching ~2000 K can be seen in the noon sector above ~350 km, while a lower temperature around 1000–1250 K is present in the midnight sector. In the dawn and dusk sectors, the sector median
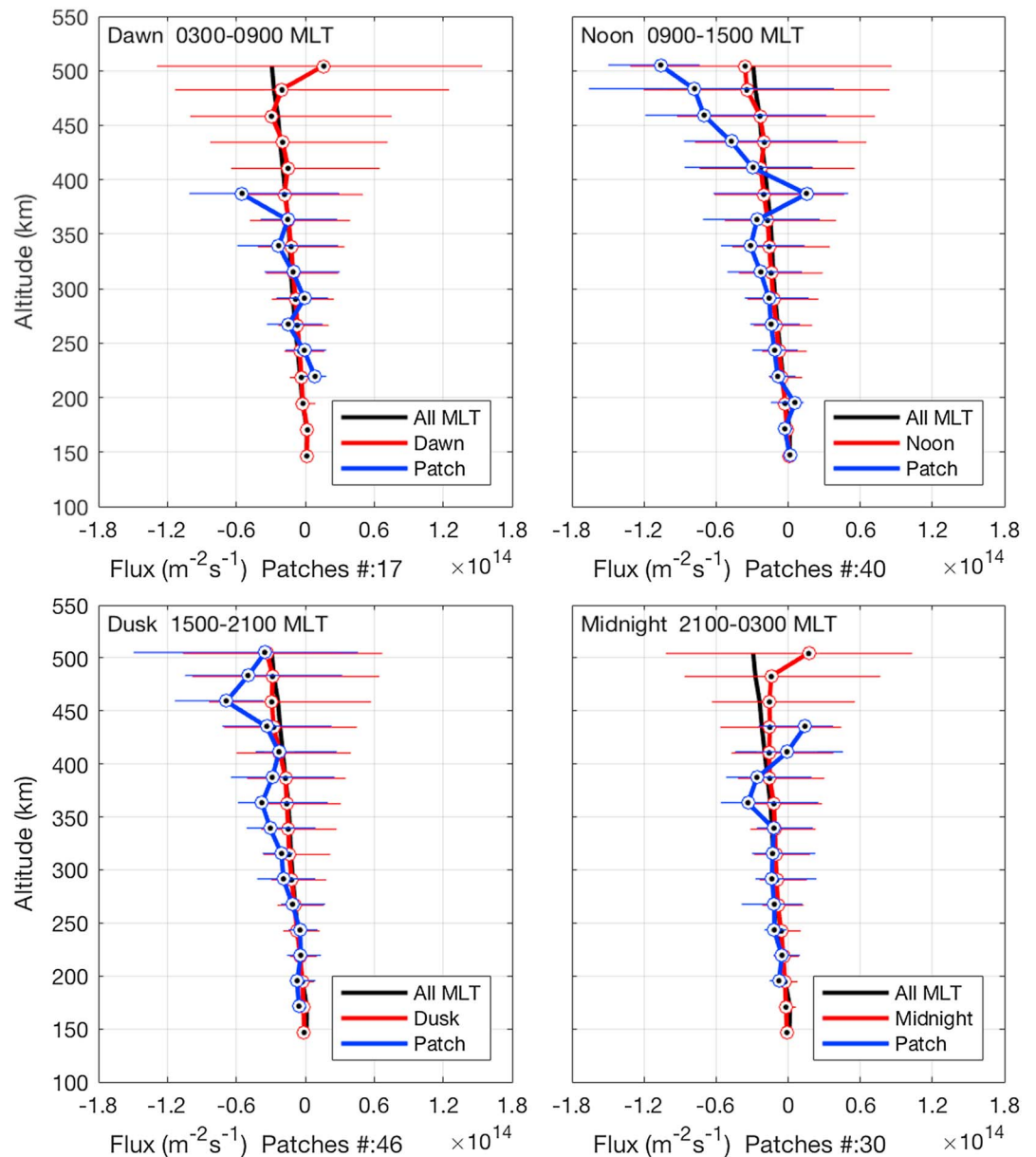
Figure 7. Line-of-sight ion flux profiles in dawn (03–09 MLT), noon (09–15 MLT), dusk (15–21 MLT) and midnight (21–03 MLT) sector, using only the vertical beam (90° elevation angle).

electron temperature profiles are closer to the overall profile. Judging from the length of the horizontal bars of the sector profiles, larger variations in the electron temperature above 200 km can be seen on the dayside than that on the nightside. Below 200 km, the midnight sector median electron temperature shows larger variations than dayside, and the horizontal bars (from Q1 to Q3) of electron temperature mainly extend to its right, which is probably due to the heating effect of particle precipitations such as polar cap arcs on the nightside.

In the noon sector, electron temperature within the patches show a clear suppression as large as ~380 K between 250 and 450 km, compared with the sector median temperature. In the midnight sector, electron temperature within the patches does not show large difference with the sector median. The results by Perry (2015, Figure 4.18) also showed patch electron temperature ~1800–2000 K in sunlit region and ~1000 K in dark region. In the dawn and dusk sectors, electron temperature within the patches is slightly lower than the sector median values, but the differences are smaller comparing with that in the noon sector.
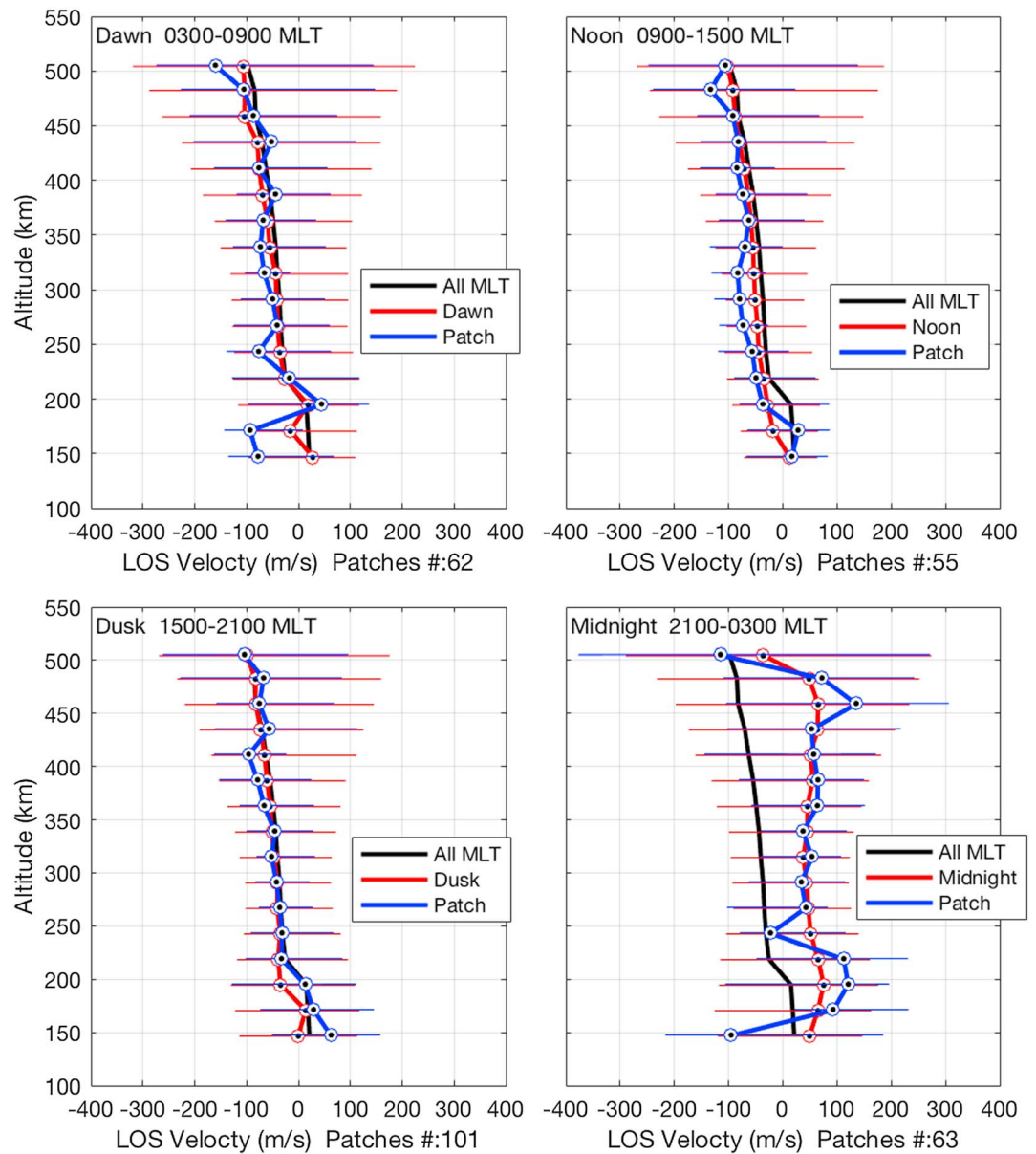
Figure 8. Line-of-sight ion velocity profiles measured in dawn (03–09 MLT), noon (09–15 MLT), dusk (15–21 MLT), and midnight (21–03 MLT) sector, using only the beam with 83° elevation angle and −157° azimuthal angle. MLT = magnetic local time.

3.2.3. Ion Temperature Profile

In general, the ion temperatures increase slowly around 1000 K as altitude increases, which are ~200 K higher than Perry (2015, Figure 4.17) reported based on data taken in 2010 near deep solar minimum. Thus, the difference is likely due to the solar cycle effect. There is little difference shown among the three ion temperature profiles in each sector. In the noon sector, the ion temperature within the patches increases to ~1230 K at ~390 km, higher than the sector median by ~150 K. This heating is likely due to stronger interaction between electrons and ions through the Coulomb collision within the patch. The Coulomb collision rate is proportional to plasma density and inversely proportional to electron temperature (Schunk & Nagy, 2009). So the colder patch electron temperature and the higher density within the patch facilitate stronger coupling between electron and ion. Combined with electron temperature measurements, the sector median T_e/T_i ratio in the noon sector can reach as large as ~1.9 between ~290 and 430 km, while within the patches the T_e/T_i ratios are only ~1.3–1.6 at the same altitudes.
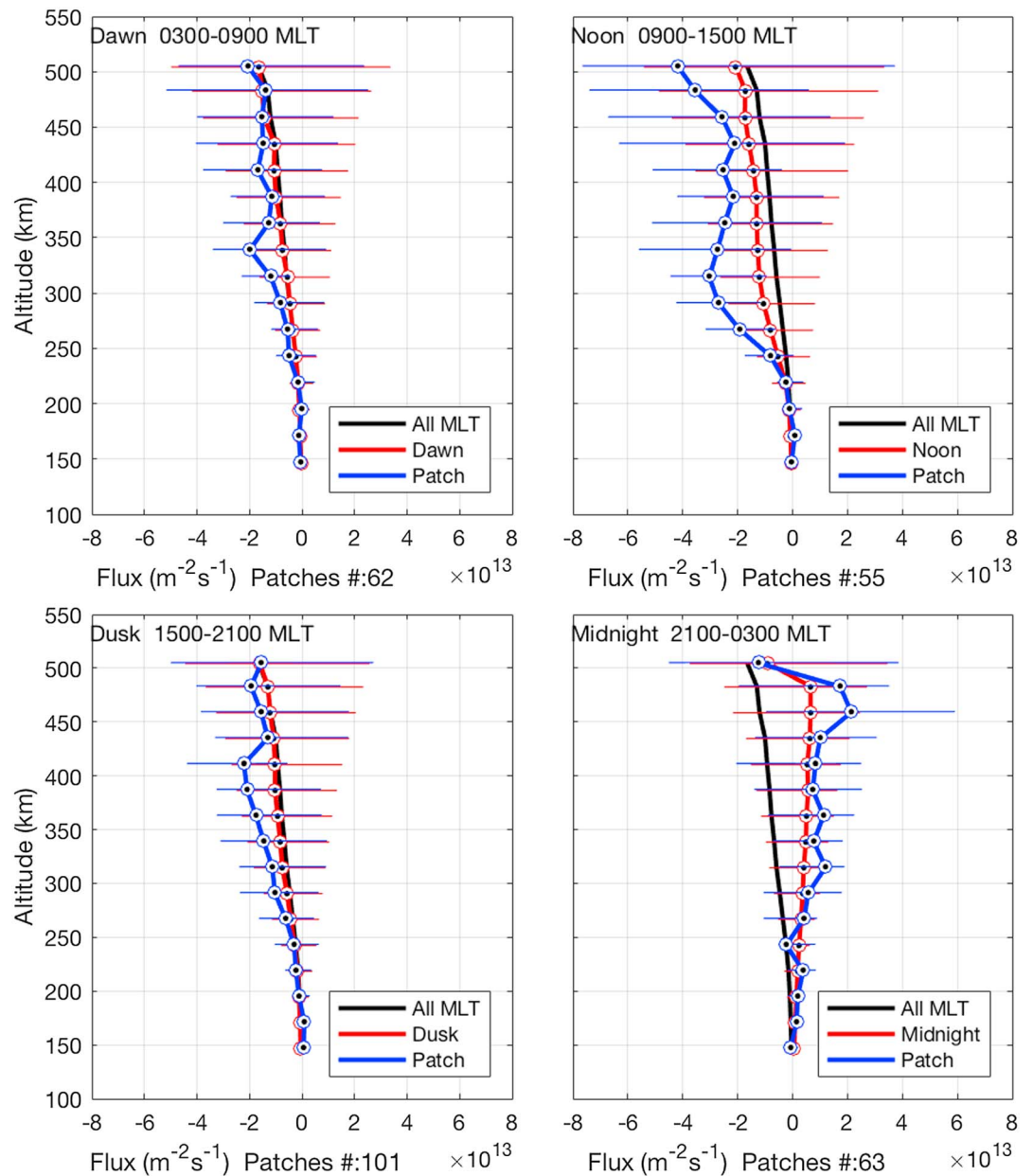
Figure 9. Line-of-sight ion fluxes profiles measured in dawn (03–09 MLT), noon (09–15 MLT), dusk (15–21 MLT), and midnight (21–03 MLT) sector, using only the beam with 83° elevation angle and −157° azimuthal angle. MLT = magnetic local time.

3.2.4. Line-of-Sight Ion Velocity and Flux Profile

As mentioned in section 2.1, the data used to calculate the statistical profiles in this study are measured by three different beams (with 90°, 83°, and 85° elevation angle, respectively) throughout the 7-month period, depending on the operation mode of the radar on each run. Specifically, the vertical beam (90° elevation) has in total ~590 hr observation time and 133 patches observed. Meanwhile, the beam with 83° elevation angle has operated for ~500 hr in total with 281 patches identified. The last beam with 85° elevation angle only has ~20 running hours and observed 23 patches. Although the second beam has less total operation hours than the vertical one, it has observed more patches, mainly because January 2016 has seen 122 patches (more than any other months in the data) and during the most of that month only the beam with 83° elevation angle was operated.

In order to study the vertical motion of the patches, at first, only data from the vertical beam are used to calculate the LOS velocity and flux profiles, shown in Figures 6 and 7. The ion flux is calculated by multiplying ion LOS velocity with electron density, assuming charge neutrality. Since only 133 patches were observed by the vertical beam, the median profiles of the patches are more fluctuating. In addition, the vertical beam of RISR-C (and RISR-N) are less sensitive than the other looking directions since they are near the grating-lobe steering limit of the phased array. For the patch profile in each MLT sector, the median values at some altitudes are not plotted if the number of available data points at that altitude level is less than 10 after applying the data quality filter.

As illustrated in Figures 6 and 7, the overall median vertical ion velocity is downward (negative) with a speed of ~60 m/s at ~300 km, causing downward fluxes ~1.1×10^{13} m^{-2} s^{-1}. The sector median profiles of vertical ion velocity are similar to the overall velocity profile. For the noon sector, the sector median flux profile presents a downward flux ~1.3×10^{13} m^{-2} s^{-1} at ~300 km because of high F2 layer density peak at dayside. Within the patches, downward ion fluxes are found between 250 and 350 km in all sectors. In the noon sector, downward ion velocity and flux within the patches can reach as large as ~66 m/s and ~3.1×10^{13} m^{-2} s^{-1} at ~340 km, respectively, while within the patches in the midnight sector, downward ion velocities can reach ~100 m/s with a downward flux of ~3.3×10^{13} m^{-2} s^{-1} at ~360 km.

In addition, the beam with 83° elevation and −157° azimuthal angle has observed 281 patches in total and therefore gives better statistical profiles of LOS ion velocity and fluxes, which are shown in Figures 8 and 9. The overall LOS ion velocity is downward and ~40 m/s at ~300 km. The overall ion flux is downward and ~5×10^{12} m^{-2} s^{-1} at ~300 km, where the density peaks. The noon sector has larger downward ion velocity ~50 m/s at ~300 km and downward ion flux ~1×10^{13} m^{-2} s^{-1} at ~300 km, while oppositely the midnight sector has upward ion velocity ~40 m/s between 200 and 400 km and upward ion flux ~4×10^{12} m^{-2} s^{-1} at ~300 km. Within the patches observed in the noon sector, downward ion velocity and flux as large as ~80 m/s and ~3×10^{13} m^{-2} s^{-1}, respectively, are found between 250 and 400 km. For patches seen in the midnight sector, upward ion velocity and flux as large as ~60 m/s and ~1.2×10^{13} m^{-2} s^{-1}, respectively, are found between 250 and 400 km.

4. Discussion

In Figure 2, we showed the occurrence frequency of the patches observed by RISR-C as a function of MLT and UT. Previous studies have reported a UT dependence of the polar cap patches occurrence in winter that more patches tend to appear during 1200–2400 UT (Coley & Heelis, 1995) or during 2000–0300 UT (David et al., 2016; Sojka et al., 1994). This is suggested to be a result of the mismatch between the geographic and geomagnetic poles (Carlson, 2012; Foster, 1993; Sojka et al., 1979) that the polar cap or cusp will extend to lower geographic latitude on the dayside during 1200–2400 UT in the NH winter; thus, more solar EUV-produced high-density plasma will be introduced into the polar cap by the ionospheric convection during this period, which is favorable to the formation of polar cap patches. In our results, more patches were observed between 2200 and 0200 UT, consistent with the findings of Sojka et al. (1994) and David et al. (2016).

As for the MLT dependence, McEwen and Harris (1996) observed more patches during local evening hours than the morning hours, using meridian-scanning photometer at Eureka (89° MLat), close to Resolute Bay (82° MLat). Noja et al. (2013) also reported higher patch occurrence on the dusk side and lower occurrence on the dawn side around 6 MLT at ~80° MLat, based on the CHAMP TEC observation from 2001 to 2004. In our results, more patches were observed between 1400 and 1900 MLT, consistent with the McEwen and Harris (1996) and Noja et al. (2013) studies.

The asymmetry of the dusk-dawn convection cells is suggested to affect patch MLT occurrence. In the polar cap, antisunward plasma flow is typically dominant during southward IMF B_z condition, while the a positive (negative) IMF B_y condition will result in a dusk-to-dawn (dawn-to-dusk) flow direction near the dayside cusp and then a dawn-to-dusk (dusk-to-dawn) flow direction at higher latitudes. In the statistical study of patch convection velocity at Resolute Bay by Hosokawa et al. (2009), they demonstrated that the dawn-dusk direction of the patches drift velocity has a clear asymmetry: The convection velocity generally has a dawn-to-dusk direction even when the IMF B_y is 0. This dawn-to-dusk convection tendency can be explained by effect of day-night conductivity gradient (Atkinson & Hutchison, 1978), and it is also supported by empirical models

(Ruohoniemi & Greenwald, 1996, 2005) and numerical simulation results (Tanaka, 2001). This statistical dawn-to-dusk convection tendency means, after the patches are generated near the dayside cusp region, more patches will move into the dusk side of the polar cap rather than the dawn side, even when IMF B_y is close to 0. Therefore, the dawn-dusk asymmetry in the patch occurrence frequency shown in Figure 2 may be due to the dawn-dusk asymmetry of high-latitude ionospheric convection pattern.

On the nightside, Moen et al. (2007) found a bell-shape patch occurrence distribution centered at ~23:25 MLT, a slight shift to the premidnight sector, at Svalbard (76° MLat) using MSP. The authors also attributed this shift to the asymmetry of the convection pattern. It should be noted that several possible reasons could cause the difference between their patch occurrence distribution over MLTs and that in the present study. In their study, emission enhancements that reached the poleward boundary of the auroral oval within the MSP field of view were counted as patches. Besides, the patch occurrence distribution has a strong dependence on latitude. According to Noja et al. (2013, Figure 4), the peak of the patch occurrence is in the dusk side at RISR latitude (~82° MLat), while for Svalbard (76° MLat) the peak is in the premidnight sector.

Therefore, we suggest that the peak of patch occurrence rate on the dusk side can be due to both the mismatch of the geographic and the geomagnetic poles and the asymmetry of dawn-dusk ionospheric convections. However, since the instrument we used is fixed on the Earth surface, the importance of these factors cannot be resolved based on the present data set.

Zou et al. (2014) found downward ion fluxes as large as ~10^{14} m^{-2} s^{-1} within the SED plume using the PFISR observation (65.4° MLat). They suggested that the downward flux could be explained by enhanced ambipolar diffusion due to increase in pressure gradient and/or large poleward thermospheric wind during storm times, which can push the plasma downward along the field lines. In the dayside lower latitude regions, the magnetic field has a smaller inclination angle, so the E × B drift velocity and the horizontal equatorward wind has a larger upward projection on vertical direction, which plays an important role in lifting and holding the plasma at high altitudes. This is also suggested to be important for the formation of high density within SED (Heelis et al., 2009; Zou et al., 2013, 2014). In our case, the elevation angle of magnetic field lines near Resolute Bay is ~86.41°. The almost vertical field lines make the E × B drift velocity and the horizontal thermospheric wind become ineffective in holding the high-density plasma within the patch. Given a typical patch E × B drift velocity being ~200–400 m/s (Hosokawa et al., 2009) and a typical antisunward thermospheric wind velocity being ~200 m/s at Resolute (Wu et al., 2017), the antisunward E × B drift contributes to ~12–25 m/s vertically upward velocity on the dayside and downward velocity on the nightside, while the antisunward thermospheric wind causes ~12 m/s vertically downward velocity on the dayside and upward on the nightside. Because the vertical projections from the antisunward E × B drift and thermospheric wind have opposite signs on the dayside and nightside, their combined effect is likely not important in affecting the vertical motions of the patches. Given ~60–100 m/s downward velocity measured within the patches using the vertical beam, we suggest that the high-density plasma within the patches move downward are mainly due to a combination of pressure gradient force and gravitational force.

As for the beam with 83° elevation and −157° azimuthal angle pointing equatorward, since it has lower elevation angle than the magnetic field lines, the antisunward E × B drift will have larger downward component when projected along this beam on the dayside and upward component on the nightside, same direction as the contribution from the antisunward thermospheric wind. Given the same typical E × B drift velocity and thermospheric wind velocity mentioned above, the E × B drift contributes ~15–30 m/s downward velocity on the dayside and upward on the nightside along this beam direction, while the thermospheric wind produces ~12 m/s velocity downward on the dayside and upward on the nightside. In total, they can lead to ~42 m/s ion velocity downward at dayside and upward at nightside, which is comparable to the results shown in Figure 8.

In short, using only the measurements from the vertical beam, we found downward ion fluxes on a scale of 10^{13} m^{-2} s^{-1} within the patches in all four sectors, likely caused by the pressure gradient force and gravity. Typical E × B drift and thermospheric wind at Resolute Bay are not large enough to lift or hold the lifted high density within patches at high altitudes, because of the high-elevation angle (86.41°) of the magnetic field lines. A tilted beam with 83° elevation angle has observed more patches and therefore provided better statistical results, which shows downward ion fluxes along the beam in dawn, noon and dusk sectors and upward ion fluxes along the beam in the midnight sector. However, the upward motion of the patches

along this beam could be partially caused by the beam's inclination and projection of the E × B drift and thermospheric wind.

5. Summary and Conclusion

In this study, we analyzed the ionospheric plasma state parameters measured by RISR-C in 2016 to firstly identify the polar cap patches and then studied their statistical characteristics, including occurrence frequency in terms of MLT, and the median vertical profiles of their plasma properties. The conclusions are summarized as follows:

1. The patches are observed more often in the afternoon sector between 1400 and 1900 MLT.
2. The density enhancement in the patches can extend from ~200 km up to above 500 km on dayside and up to ~450 km on nightside. The ratio of F-region density peak between the patches median and the sector median is ~1.8 on the dayside and ~2.1 on the nightside. Below ~200 km, the patches median density is lower than the sector median density except in the midnight sector.
3. Electron temperature within the patches is lower than the sector median in the noon, dusk, and dawn sectors, and the difference is as large as ~380 K in the noon sector, which suggests that the main plasma source of the patches is solar EUV-produced plasma in the dayside subauroral region rather than soft particle precipitation. Smaller electron temperature decrease within the patches is found in the dawn and dusk sectors comparing with that in the noon sector.
4. In the noon sector, ion temperature within the patches is higher than the sector median by ~175 K. We suggest that this is due to stronger coupling between the electrons and ions within patches due to higher Coulomb collision frequency. No significant differences between the ion temperature within the patch and sector median are found in the other sectors. The median T_e/T_i ratio in the noon sector can reach as large as ~1.9 between ~290–430 km, while within the patches the T_e/T_i ratio is ~1.3–1.6 at the those altitudes.
5. Downward ion fluxes on a scale of $\sim 10^{13}\,\mathrm{m}^{-2}\,\mathrm{s}^{-1}$ are observed within the patches in all the sectors, which are likely due to the combination of pressure gradient and gravitational forces.

It should be noted that the above results are based on the first year of RISR-C data. The patch identification algorithm and statistical analysis presented in this paper will be applied to a more comprehensive data set in the future as RISR-C continues to collect more data. In particular, more field-aligned beam observations have been scheduled, which will improve the field-aligned velocity and flux statistics in the future.

References

Anderson, D. N., Buchau, J., & Heelis, R. A. (1988). Origin of density enhancements in the winter polar cap ionosphere. *Radio Science, 23*(4), 513–519. https://doi.org/10.1029/RS023i004p00513

Atkinson, G., & Hutchison, D. (1978). Effect of the day night ionospheric conductivity gradient on polar cap convective flow. *Journal of Geophysical Research, 83*(A2), 725–729. https://doi.org/10.1029/JA083iA02p00725

Basu, S., MacKenzie, E., & Basu, S. (1988). Ionospheric constraints on VHF/UHF communications links during solar maximum and minimum periods. *Radio Science, 23*(3), 363–378. https://doi.org/10.1029/RS023i003p00363

Basu, S., MacKenzie, E., Costa, E., Fougere, P., Carlson, H., & Whitney, H. (1987). 250 MHz/GHz scintillation parameters in the equatorial, polar, and auroral environments. *IEEE Journal on Selected Areas in Communications, 5*(2), 102–115. https://doi.org/10.1109/JSAC.1987.1146533

Carlson, H. C. (2012). Sharpening our thinking about polar cap ionospheric patch morphology, research, and mitigation techniques. *Radio Science, 47*, RS0L21. https://doi.org/10.1029/2011RS004946

Carlson, H. C., Moen, J., Oksavik, K., Nielsen, C., McCrea, I. W., Pedersen, T., & Gallop, P. (2006). Direct observations of injection events of subauroral plasma into the polar cap. *Geophysical Research Letters, 33*, L05103. https://doi.org/10.1029/2005GL025230

Coley, W. R., & Heelis, R. A. (1995). Adaptive identification and characterization of polar ionization patches. *Journal of Geophysical Research, 100*(A12), 23,819–23,827. https://doi.org/10.1029/95JA02700

Crowley, G. (1996). Critical review of ionospheric patches and blobs. *Review of Radio Science, 1993–1996*, 619–648.

David, M., Sojka, J. J., Schunk, R. W., & Coster, A. J. (2016). Polar cap patches and the tongue of ionization: A survey of GPS TEC maps from 2009 to 2015. *Geophysical Research Letters, 43*, 2422–2428. https://doi.org/10.1002/2016GL068136

Foster, J. C. (1993). Storm time plasma transport at middle and high latitudes. *Journal of Geophysical Research, 98*(A2), 1675–1689. https://doi.org/10.1029/92JA02032

Foster, J. C., Coster, A. J., Erickson, P. J., Holt, J. M., Lind, F. D., Rideout, W., et al. (2005). Multiradar observations of the polar tongue of ionization. *Journal of Geophysical Research, 110*, A09S31. https://doi.org/10.1029/2004JA010928

Gillies, R. G., van Eyken, A., Spanswick, E., Nicolls, M. J., Kelly, J., Greffen, M., et al. (2016). First observations from the RISR-C incoherent scatter radar. *Radio Science, 51*, 1645–1659. https://doi.org/10.1002/2016RS006062

Heelis, R. A., Sojka, J. J., David, M., & Schunk, R. W. (2009). Storm time density enhancements in the middle-latitude dayside ionosphere. *Journal of Geophysical Research, 114*, A03315. https://doi.org/10.1029/2008JA013690

Hosokawa, K., Kashimoto, T., Suzuki, S., Shiokawa, K., Otsuka, Y., & Ogawa, T. (2009). Motion of polar cap patches: A statistical study with all-sky airglow imager at Resolute Bay, Canada. *Journal of Geophysical Research, 114*, A04318. https://doi.org/10.1029/2008JA014020

Lockwood, M., & Carlson, H. C. (1992). Production of polar cap electron density patches by transient magnetopause reconnection. *Geophysical Research Letters*, *19*(17), 1731–1734. https://doi.org/10.1029/92GL01993

McEwen, D. J., & Harris, D. P. (1996). Occurrence patterns of F layer patches over the north magnetic pole. *Radio Science*, *31*(3), 619–628. https://doi.org/10.1029/96RS00312

Moen, J., Gulbrandsen, N., Lorentzen, D. A., & Carlson, H. C. (2007). On the MLT distribution of F region polar cap patches at night. *Geophysical Research Letters*, *34*, L14113. https://doi.org/10.1029/2007GL029632

Noja, M., Stolle, C., Park, J., & Lühr, H. (2013). Long-term analysis of ionospheric polar patches based on CHAMP TEC data. *Radio Science*, *48*, 289–301. https://doi.org/10.1002/rds.20033

Perry, G. W. (2015). Large scale plasma density perturbations in the polar F-region ionosphere, (Doctoral dissertation). Retrieved from eCommons. (http://hdl.handle.net/10388/ETD-2015-02-1947). Saskatoon: University of Saskatchewan.

Rodger, A. S., Pinnock, M., Dudeney, J. R., Baker, K. B., & Greenwald, R. A. (1994). A new mechanism for polar patch formation. *Journal of Geophysical Research*, *99*(A4), 6425–6436. https://doi.org/10.1029/93JA01501

Ruohoniemi, J. M., & Greenwald, R. A. (1996). Statistical patterns of high-latitude convection obtained from Goose Bay HF radar observations. *Journal of Geophysical Research*, *101*(A10), 21,743–21,763. https://doi.org/10.1029/96JA01584

Ruohoniemi, J. M., & Greenwald, R. A. (2005). Dependencies of high-latitude plasma convection: Consideration of interplanetary magnetic field, seasonal, and universal time factors in statistical patterns. *Journal of Geophysical Research*, *110*, A09204. https://doi.org/10.1029/2004JA010815

Schunk, R., & Nagy, A. (2009). *Ionospheres: Physics, plasma physics, and chemistry*. Cambridge, UK: Cambridge University Press. https://doi.org/10.1017/CBO9780511635342

Sojka, J. J., Bowline, M. D., & Schunk, R. W. (1994). Patches in the polar ionosphere: UT and seasonal dependence. *Journal of Geophysical Research*, *99*(A8), 14,959–14,970. https://doi.org/10.1029/93JA03327

Sojka, J. J., Bowline, M. D., Schunk, R. W., Decker, D. T., Valladares, C. E., Sheehan, R., et al. (1993). Modeling polar cap F-region patches using time varying convection. *Geophysical Research Letters*, *20*(17), 1783–1786. https://doi.org/10.1029/93GL01347

Sojka, J. J., Raitt, W. J., & Schunk, R. W. (1979). Effect of displaced geomagnetic and geographic poles on high-latitude plasma convection and ionospheric depletions. *Journal of Geophysical Research*, *84*(A10), 5943–5951. https://doi.org/10.1029/JA084iA10p05943

Spicher, A., Clausen, L. B. N., Miloch, W. J., Lofstad, V., Jin, Y., & Moen, J. I. (2017). Interhemispheric study of polar cap patch occurrence based on Swarm in situ data. *Journal of Geophysical Research: Space Physics*, *122*, 3837–3851. https://doi.org/10.1002/2016JA023750

Tanaka, T. (2001). Interplanetary magnetic field B_y and auroral conductance effects on high-latitude ionospheric convection patterns. *Journal of Geophysical Research*, *106*(A11), 24,505–24,516. https://doi.org/10.1029/2001JA900061

Tsunoda, R. T. (1988). High-latitude F region irregularities: A review and synthesis. *Reviews of Geophysics*, *26*(4), 719–760. https://doi.org/10.1029/RG026i004p00719

Wang, B., Nishimura, Y., Lyons, L. R., Zou, Y., Carlson, H. C., Frey, H. U., & Mende, S. B. (2016). Analysis of close conjunctions between dayside polar cap airglow patches and flow channels by all-sky imager and DMSP. *Earth, Planets and Space*, *68*(1), 150. https://doi.org/10.1186/s40623-016-0524-z

Weber, E. J., Buchau, J., Moore, J. G., Sharber, J. R., Livingston, R. C., Winningham, J. D., & Reinisch, B. W. (1984). F layer ionization patches in the polar cap. *Journal of Geophysical Research*, *89*, 1683–1694. https://doi.org/10.1029/JA089iA03p01683

Wu, Q., Jee, G., Lee, C., Kim, J.-H., Kim, Y. H., Ward, W., & Varney, R. H. (2017). First simultaneous multistation observations of the polar cap thermospheric winds. *Journal of Geophysical Research: Space Physics*, *122*, 907–915. https://doi.org/10.1002/2016JA023560

Zhang, Q.-H., Zhang, B. C., Liu, R. Y., Dunlop, M. W., Lockwood, M., Moen, J., et al. (2011). On the importance of interplanetary magnetic field |B_y| on polar cap patch formation. *Journal of Geophysical Research*, *116*, A05308. https://doi.org/10.1029/2010JA016287

Zou, S., Moldwin, M. B., Ridley, A. J., Nicolls, M. J., Coster, A. J., Thomas, E. G., & Ruohoniemi, J. M. (2014). On the generation/decay of the storm-enhanced density plumes: Role of the convection flow and field-aligned ion flow. *Journal of Geophysical Research: Space Physics*, *119*, 8543–8559. https://doi.org/10.1002/2014JA020408

Zou, S., Ridley, A. J., Moldwin, M. B., Nicolls, M. J., Coster, A. J., Thomas, E. G., & Ruohoniemi, J. M. (2013). Multi-instrument observations of SED during 24–25 October 2011 storm: Implications for SED formation processes. *Journal of Geophysical Research: Space Physics*, *118*, 7798–7809. https://doi.org/10.1002/2013JA018860

Zou, Y., Nishimura, Y., Lyons, L. R., Shiokawa, K., Donovan, E. F., Ruohoniemi, J. M., et al. (2015). Localized polar cap flow enhancement tracing using airglow patches: Statistical properties, IMF dependence, and contribution to polar cap convection. *Journal of Geophysical Research: Space Physics*, *120*, 4064–4078. https://doi.org/10.1002/2014JA020946